Journal of Molecular Structure 1305 (2024) 137789

Contents lists available at ScienceDirect

Journal of Molecular Structure

journal homepage: www.elsevier.com/locate/molstr

# Study of microstructure, magnetic and gas sensing properties of porous $Ni_{0.4+x}Zn_{0.6-x}Ce_yFe_{2-y}O_4$ magnetic nanoparticles

Sanele T. Dlamini [a,b], Thomas Moyo [a], Amos Nhlapo [c,*], Daniel Wamwangi [d], Amos Akande [e,f], Bonex W. Mwakikunga [g,h]

[a] School of Chemistry and Physics, University of KwaZulu-Natal, Westville Campus, Private Bag X54001, Durban, South Africa
[b] School of Chemicals and Physical Sciences, Faculty of Agriculture and Natural Science, University of Mpumalanga, Mbombela 1200, South Africa
[c] Department of Medical Physics, Sefako Makgatho Health Sciences University, Medunsa, P.O. Box 146, 0204, South Africa
[d] Material Physics Research institute and School of Physics, University of the Witwatersrand, Wits, Private Bag 3, Johannesburg 2050, South Africa
[e] EDT4IR Research Centre, CSIR-NexGen Enterprises and Institutions Cluster, P.O. Box 395, Pretoria 0001, South Africa
[f] School of Physics, Institute of Photonics and Optical Science, The University of Sydney, Camperdown, NSW 2006, Australia
[g] DST/CSIR-National Centre for Nano-Structured Materials, P.O. Box 395, Pretoria 0001, South Africa
[h] Department of Physics, Arcadia Campus, Tshwane University of Technology, Pretoria 0001, South Africa

ARTICLE INFO

*Keywords:*
Glycol-thermal synthesis
Spinel ferrites
Magnetization
Mossbauer spectroscopy
Gas sensing

ABSTRACT

The spinel ferrite systems$Ni_{0.4+x}Zn_{0.6-x}Ce_yFe_{2-y}O_4$ ($0 \leq x+y \leq 0.3$) were synthesized by a modified glycol-thermal technique. X-ray diffractometer (XRD) confirmed formation of single phase cubic spinel structure with average crystallite sizes 8–21 nm. The crystallite sizes were found to be in agreement with the particle sizes obtained from the high resolution transmission electron microscopy (HRTEM) indicating formation of single domain nanoparticles. Scanning electron microscopy (SEM) showed a homogeneous spread of semi-spherical nanoparticles. Brunauer-Emmett-Teller (BET) revealed specific surface area ranging between 64 and 108 $m^2/g$, while Barrett-Joyner-Halenda (BJH) showed the pore sizes varying between 48 and 126 nm. Cation distribution obtained from Rietveld refinement revealed all $Ce^{3+}$ occupied B- sites whilst $Ni^{2+}$, $Zn^{2+}$, $Fe^{3+}$ occupied both A and B sites. Magnetization measurements were performed using the vibration samples magnetometer (VSM). The saturation magnetization varied between 51 and 60 emu/g, while the coercivity dropped from 114 to 89Oe. The remnant magnetization varied between 3 and 12 emu/g. A correlation was observed between the saturation magnetization and the effective magnetic moments confirming cation distribution to be reliable. A strong correlation between initial susceptibility and unit cell volume was found. The crystallite sizes varied inversely with initial magnetic susceptibility. The magnetic characteristics of presented materials make them useful in high frequency device applications and has potential use as contrast agent in magnetic resonance imaging (MRI). $^{57}Fe$ Mössbauer spectroscopy revealed the strengthening of ferromagnetic coupling. Gas sensing tests revealed a decrease in sensing response with the transition from paramagnetic state to ferromagnetic state. The $Ni_{0.4}Zn_{0.6}Fe_2O_4$ sample showed the best sensing response to $SO_2$ at 100 °C compared to CO gas. However, at 150 °C the sample was more sensitive to CO gas than $SO_2$ gas.

## 1. Introduction

Spinel ferrite materials have been widely investigated in recent years due to their remarkable electrical and magnetic properties. These attributes render them suitable for diverse applications, including information storage systems, refrigeration, gas sensing, high infrequency devices, ferro-fluid technology, magneto-caloric refrigeration and medical diagnosis [1,2]. Spinel ferrites are of the general formula $AB_2O_4$, where A represent divalent metal ions and B is a trivalent metal ions that reside in the 8 tetrahedral and 16 octahedral sites of the spinel lattice, respectively [1]. The distribution of cations between the A and B sites categorizes spinels as normal, inverse, or mixed. The cations distribution play a role in determining the magnetic state of the ferrites. It is the dual property of electric and magnetic effects exhibited by these materials that has spurred extensive research for a variety of application in both bulk and nano-sized dimensions [3]. These properties are

* Corresponding author.
*E-mail address:* amos.nhlapo@smu.ac.za (A. Nhlapo).

https://doi.org/10.1016/j.molstruc.2024.137789
Received 8 November 2023; Received in revised form 23 January 2024; Accepted 10 February 2024
Available online 11 February 2024

heavily influenced by synthesis techniques, structural changes, cation distribution and composition, stoichiometry, and annealing conditions [4–7]. Conduction in spinel ferrites occurs via charge carriers (electrons or holes) that can transfer between cations [8].

The unique magnetic and electrical properties of the soft magnetic semiconducting Ni-Zn ferrites make it one of the most versatile materials associated tuneable magnetic properties for applications such as magnetic transformer cores, high frequency devices, contrast agents in magnetic resonance imaging (MRI), filters, read/write magnetic heads and isolators [9–11]. Furthermore, soft magnetic Ni-Zn ferrites have been reported to have a degree of sensing for reducing gases [12–15]. In general, a material with a high surface area is required to have effective gas sensing characteristics, and Ni-Zn ferrites possess these characteristics [16]. The magnetic and gas sensing characteristics of Ni-Zn ferrites nanoparticles rely significantly on factors such as morphology, composition, surface charge density. These properties are sensitive to the preparation methodology employed during their synthesis.

Rare-earth (RE) metals possess unpaired 4f electrons, and their substitution in spinel ferrites, induces interactions between Fe-RE ions. This interaction leads to alterations in structural parameters such as particle size and surface strain resulting, consequently impacting various physical properties [1]. The magnetic interactions and electrical resistivity of ferrimagnetic or ferromagnetic materials are typically governed by interactions between Fe-Fe ions. The introduction of RE ions into the spinel crystal lattice of a ferri/ferro-magnetic materials, initiates an interaction between Fe-RE ions, resulting in changes in the magnetic and electrical properties of the ferrites [17]. This is expected to significantly modify the magnetic characteristics and influence gas sensing properties. Therefore, by substituting $RE^{3+}$ions, it becomes possible to modify the magnetic characteristics of Ni-Zn ferrites. However, RE ions exhibit a low solubility limit in spinel ferrite and can easily form secondary orthoferrite-phase ($REFe_2O_4$) beyond their limit. The formation of secondary phase can negatively affect the magnetic and sensing properties. To mitigate this, a careful approach involves introducing a small amount of RE ions and selecting an appropriate synthesis method to stabilize the RE ions within the spinel structure [18].

The properties of ferrite nanoparticles are influenced by composition and microstructure, both of which are sensitive to synthesis method. A number of researchers have investigated the structure, magnetic and gas sensing properties of spinel ferrites [19–22]. O. Abd-Elkader et al. [23], investigated the structure, magnetic and gas sensing characteristic of $CoW_xFe_{2-2x}O_4$ ferrites synthesized by sol-gel method. They reported increased magnetization at low concentrations of $W^{4+}$ ions. The magnetization decreased with an increase in the concentration of $W^{4+}$ ions. This reduction was associated with the redistributions of Fe ion on tetrahedral and octahedral sites. They further reported that $CoW_{0.15}Fe_{1.97}O_4$ is better suited for detecting for acetone gas sensing at 200 °C compared to ammonia and ethanol. Joshi et al. [24], explored the impact of Ni substitution on the gas sensing properties of cobalt ferrites synthesized by co-precipitation method. They discovered that the introduction of $Ni^{2+}$ ions into cobalt ferrite exhibited a preferred selectivity for CO gas at higher temperature of 325 °C and ethanol gas at relatively low temperature of 250 °C. They also observed that both undoped cobalt ferrite and undoped nickel ferrite exhibit a comparable response for both these CO and ethanol gases. Qayoom et al. [25], used the combustion method to synthesize $Ni_{0.5}Zn_xMg_{0.5-x}Fe_2O_4$ ferrites. They investigated the structural characteristics and the gas sensing properties towards ammonium ($NH_3$) at room temperature. They concluded that $Ni_{0.5}Zn_xMg_{0.5-x}Fe_2O_4$ ferrites are effective for detecting ammonia vapor at room temperature. The response of spinel ferrites to reducing gases is inherently unpredictable. The gas sensing response is influenced by not only morphology but also by material composition, cation distribution, type of gas, gas concentration, operating temperature, synthesis technique, and the material microstructure [16,26]. It is well known that in most materials, the electron interaction has a much stronger effect than the magnetic interaction for gas sensing. Magnetic interactions can influence the electrical properties of a material [27]. However, the relation between the sensing and the magnetic properties is still yet to be understood.

Various synthesis methods, such as glycol-thermal and sol-gel [28], co-precipitation [29], ball milling [30], hydrothermal [31], refluxing [32], and auto-combustion [33], have been employed to fabricate ferrite nanoparticles. Development of high quality ferrites materials at economical costs to meet specific application requirements poses a continuous challenge for researchers. Among various synthesis techniques, the glycol-thermal method has garnered significant attention due to its advantages, particularly its ability to generate smaller particle sizes. Moreover, the glycol-thermal method is recognized as a cost-effective, simple, and efficient approach for producing a diverse range of ferrite materials.

This work reports the effect of substituting $Ce^{3+}$ ions while varying the fractional population of nickel and zinc at the A and B sites on structural, magnetic, and gas sensing properties. $Ce^{3+}$ ions are hardly influenced by the surrounding ions due to the 4*f* shell being well shielded by the $5s^25p^6$ layer of electrons. The Ce-Fe interaction in Ni-Zn ferrites is said to be caused by the occurrence of 4*f* - 3d couplings with due to addition of $Ce^{3+}$ ions [34]. Therefore, the substitution of Ce in Ni-Zn ferrite is expected to alter the magnetic properties. The materials were further tested for their sensing response to $SO_2$ and CO gases.

## 2. Experimental

### 2.1. Materials and synthesis procedure

A series of samples $Ni_{0.4}Zn_{0.6}Fe_2O_4$ (S1), $Ni_{0.4}Zn_{0.6}Ce_{0.1}Fe_{1.9}O_4$ (S2), $Ni_{0.6}Zn_{0.4}Ce_{0.1}Fe_{1.9}O_4$ (S3), and $Ni_{0.5}Zn_{0.5}Ce_{0.1}Fe_{1.9}O_4$ (S4) were fabricated via a modified glycol-thermal technique. Stoichiometric amounts of $NiCl_2$ (98 %), $ZnCl_2$ (98 %), $CeCl_37H_2O$ (99.9 %) and $FeCl_36H_2O$ (98 %) were dissolved in 100 mL of deionised water. The pH of the solution was adjusted to about 10 by gradual addition of ammonium hydroxide solution under vigorous stirring using a magnetic stirrer. The formed precipitate was washed several times with deionized water using filtration method. The cleaned precipitate (without presence of chlorides) was dissolved into a 300 mL of ethylene glycol and transferred into a glass lining in a 600 mL stain- less steel pressure vessel (Watlow series model PARR 4843 reactor). The solution was stirred at 300 rpm at 200 °C for 6 h. The reaction pressure was allowed to rise to 100 psi. The glycol-reacted precipitate was washed again using deionized water. The obtained samples were heated in an oven at 200 °C for 4 h in air atmosphere and finally quenched to room temperature to obtain the as-prepared samples.

### 2.2. Characterization techniques

X-ray diffraction (XRD) analysis was performed for phase identification using Cu-Kα radiation ($\lambda = 1.5406$ Å) on a Bruker D8 Advance diffractometer in the Bragg-Brentano Geometry. The microstructure and morphology were investigated using a Joel JEM2100 high-resolution transmission electron microscopy (HRTEM) and a Zeiss Evo LS15 scanning electron microscopy (SEM). BET and BJH were used to determine specific surface areas and average pore sizes. Measurements were conducted at 77 K on a Tristar II instrument manufactured by Micromeritics (USA). A Renishaw in Via Raman microscopy was used to investigate structural configurations and confirm spinel structure. Room temperature $^{57}Fe$ Mössbauer spectroscopy was used to extract information about the magnetic interaction, and the oxidation state of Fe ions. A Physical Property Measurement system DynaCool 12 T equipped with a vibrating sample magnetometer (VSM) was used to determine the room temperature magnetic properties. Gas sensor fabrications and tests were performed on a KSGA565 KENOSISTEC instrument from Italy, as described previously [35].

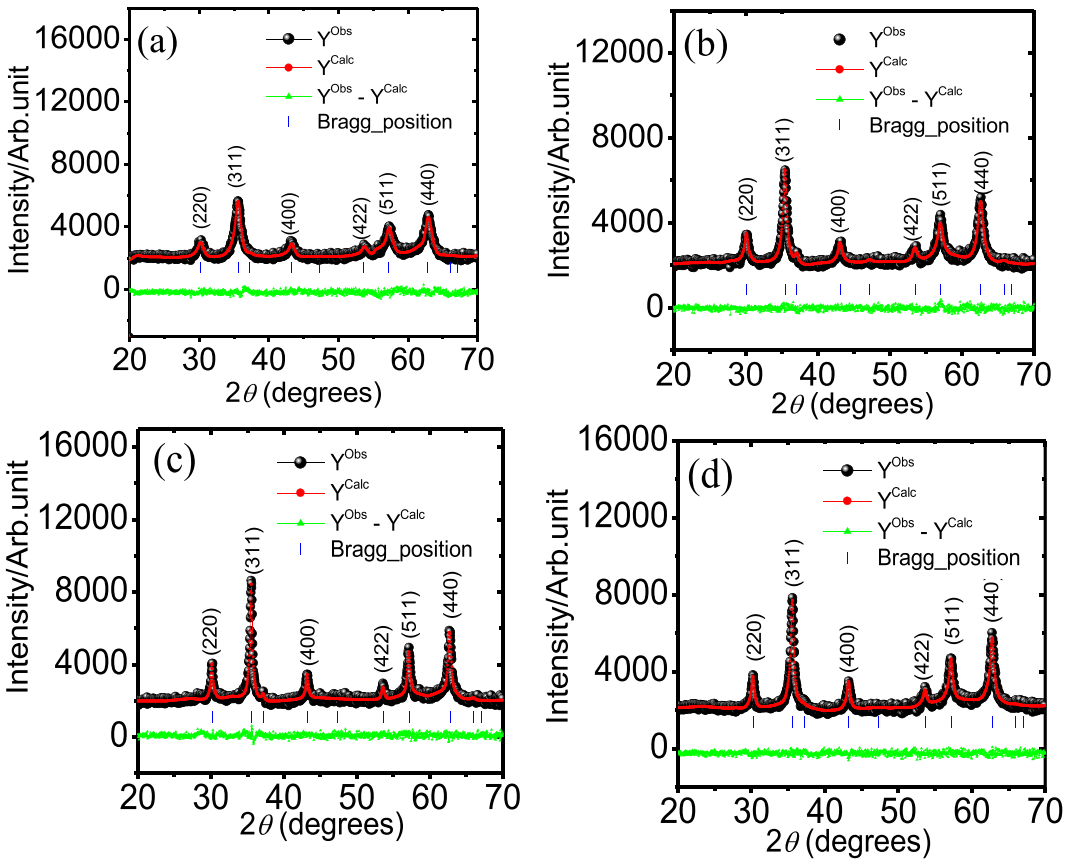


**Fig. 1.** Rietveld refined XRD pattern of samples S1(a), S2 (b), S3 (c), and S4 (d).

**Table 1**
Synthesized $Ni_{0.4+x}Zn_{0.6-x}Ce_yFe_{2-y}O_4$ samples with corresponding labels.

| *x* | *y* | Composition | Sample labels |
|---|---|---|---|
| 0 | 0 | $Ni_{0.4}Zn_{0.6}Fe_2O_4$ | S1 |
| 0 | 0.1 | $Ni_{0.4}Zn_{0.6}Ce_{0.1}Fe_{1.9}O_4$ | S2 |
| 0.1 | 0.1 | $Ni_{0.5}Zn_{0.5}Ce_{0.1}Fe_{1.9}O_4$ | S3 |
| 0.2 | 0.1 | $Ni_{0.6}Zn_{0.4}Ce_{0.1}Fe_{1.9}O_4$ | S4 |

## 3. Results and discussions

### 3.1. Structural and morphology analysis

The crystal structure of the samples were analysed by Rietveld refinement using the *Fullprof Suite* software package on the collected XRD patterns [36]. The model for refinement was based on assumed $Zn^{2+}$ and a fraction of $Fe^{3+}$ ions occupied tetrahedral sites whilst $Ce^{3+}$, $Ni^{2+}$ and the other fraction of $Fe^{3+}$ ions all occupied the octahedral sites. The atomic occupation fractions at tetrahedral 8*a* (1/8,1/8,1/8) and octahedral 16*d* (1/2,1/2,1/2) Wyckoff sites were refined in mutual constraint to avoid over or under population of specific sites [37]. The atomic positions of oxygen ( *u*), at the 32*e* Wyckoff sites, were refined along with the lattice parameters (*a*). Fig. 1 show the XRD patterns of the samples labelled S1, S2, S3 and S4 and their corresponding compositions in Table 1.

The refined XRD patterns show pure single-phase cubic spinel structures belonging to the space group$Fd\bar{3}m$. The quality of the fits to the experimental data is satisfactory. The goodness of fit $\chi^2$, profile experimental and weighted reliability index factors $R_{exp}(\%)$ and $R_{wp}(\%)$ respectively are recorded in Table 2 together with other structural parameters. These values are within the range of reported values in the literature [38–41]. The crystallite sizes based on the refined data were calculated using the Scherer formula $t_{XRD} = \frac{k\lambda}{\beta\cos\theta}$ where $\lambda$ is the X-ray beam wavelength, $\theta$ is the Bragg's angle, $\beta$ describes the peak broadening characterized by the full width at half maxima of the most intense 311 peak, and *k* is the shape factor set to be 0.94 [42]. Fig. 2 shows the polyhedron of the refined crystal structure corresponding to the S4 XRD pattern [26].

The XRD crystallite and TEM particle sizes in Fig. 3(a) are shown to be roughly of equal sizes which show consistence in the two measurements. The variation of the lattice parameter *a* in Fig. 3(b) appears to be significantly influenced by the substitution of smaller size $Fe^{3+}$ ions (ionic radius 0.64 Å) by larger $Ce^{3+}$ ions (1.01 Å) which accounts for increased *a* for S2. Lower values of *a* with Ce substitution for samples S3

**Table 2**
Particle sizes ($t_{TEM}$) from HRTEM images, Rietveld refined crystallite sizes ( $t_{XRD}$), full widths at half maximum ( $\beta$), density ( $\rho$), cubic cell volume ( $V_0$), lattice parameter ( *a*), the goodness of fit parameter ( $\chi^2$), profile experimental reliability index factor ( $R_{exp}$) and profile weighted reliability index factors ( $R_{wp}$).

| Sample | $t_{TEM}$(nm) | $t_{XRD}$ (nm) | $\beta$ | $\rho$ (g/cm3) | $V_0$ (Å3) | *a* (Å) | $\chi^2$ | $R_{exp}$(%) | $R_{wp}$ (%) |
|---|---|---|---|---|---|---|---|---|---|
| S1 | 8.1(1) | 7.9(1) | 0.33 | 5.417 | 584.68(9) | 8.36192(8) | 1.31 | 10 | 13 |
| S2 | 12.6(2) | 11.3(5) | 0.46 | 5.565 | 587.15(6) | 8.38315(5) | 1.47 | 12 | 15 |
| S3 | 21.1(4) | 19.5(5) | 0.84 | 5.820 | 586.17(3) | 8.36899 (2) | 1.32 | 10 | 12 |
| S4 | 15.9(1) | 13.2(3) | 0.58 | 5.929 | 585.17(4) | 8.36424 (3) | 1.15 | 09 | 11 |

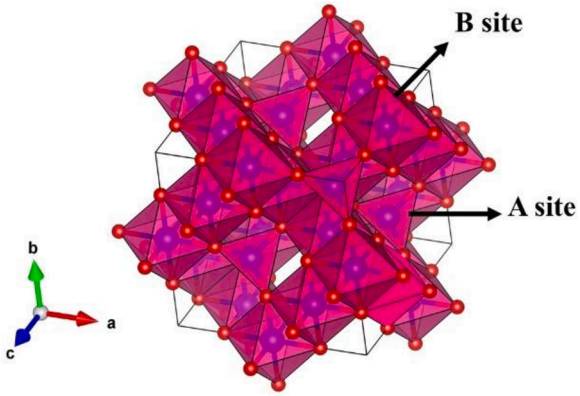


**Fig. 2.** Illustration of a cubic spinel structure (space group$Fd\bar{3}m$) based on XRD pattern of S4. The illustration was created using the structural visualization software *VESTA* [26].

and S4 can be attributed to reduced content of larger $Zn^{2+}$ ions (0.74 Å) due to substitution by smaller $Ni^{2+}$ ions (0.69 Å) [43]. This can be justified numerically by assuming that increments in lattice parameters depend linearly on ionic radii $r_i$ and concentrations of substituting ions ($x$ and $y$). In the present case for $Ni_{0.4+x}Zn_{0.6-x}Ce_yFe_{2-y}O_4$ with increased $Ce^{3+}$ and $Ni^{2+}$, we may assume increments in the form of

$$\Delta a = A_1(r_{Ce} - r_{Fe})y + A_2(r_{Ni} - r_{Zn})x \quad (1)$$

where $A_i$ are constants associated with substitutions at octahedral and tetrahedral sites.

For$A_1 \approx A_2 = A$, the parameter $\Delta a/A \approx 0$, 0.037, 0.032 and 0.027 Å for $x + y = 0$, 0.1, 0.2 and 0.3 respectively that confirms the trend foain Fig. 3(b).

The substitutions can also cause distortion in the crystal lattice of the host compound that can lead to the formation of pseudo-cubic phases and enhancement of the lattice parameters. From the Rietveld refinement results of XRD patterns, full width at half maximum (FWHM) given in Table 2 increased with the introduction of $Ce^{3+}$ and increased $Ni^{2+}$ ions that may indicate increased stacking faults and some structural disorder [28]. The average bond lengths are recorded in Table 3 were extracted from the *BondStr* program included in the *Fullprof Suite* software package. The values are in agreement with those reported in the literature [29,30]. Other calculated parameters from the package are given in Table 4. These include average bond lengths on A and B sites presented in Fig. 4(a). A decrease in $R_A$ from S1 to S2 is attributed to the changes due to the introduction of $Ce^{3+}$ ions into the Ni-Zn spinel structure causing relative displacement of the oxygen ions at the B sites and produce shrinkage in bond length at the A sites. This shrinkage is largely linked to more covalent bonding of cation-anions at A sites compared to the B sites [31]. However, at higher $Ni^{2+}$ content between S3 and S4, there is a decrease in bond length $R_B$ and an increase in$R_A$. This may indicate more covalent bonding at the B sites in comparison to the A sites [41]. The magnetic ion hopping lengths $L_A$ and $L_B$ are also given in Table 4 and plotted as a function of $x + y$ in Fig. 4(b) appear to correlate well with lattice constants and differences in ionic radii of constituent ions.

The refined oxygen positional parameter ($u$) given in Table 4 and

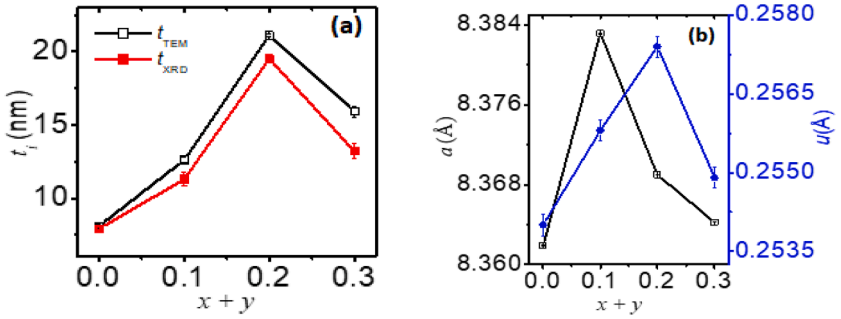


**Fig. 3.** (a) Compositional dependences of crystallite sizes $t_{XRD}$ and particle sizes $t_{TEM}$ for samples S1–S4. (b) The compositional variation of lattice constants $a$and oxygen positional parameters (μ).

**Table 3**
Bond structure for samples S1–S4 obtained from the *BondStr* program distributed within the *Fullprof Suite* software.

| Bonds | S1 (Å) | S2 (Å) | S3 (Å) | S4 (Å) |
|---|---|---|---|---|
| (O) - (O) | 3.5154(14) | 3.0154(13) | 3.1336(8) | 3.0732(8) |
| (O) - ($Fe^A$) | 1.8683(5) | 1.7884(6) | 1.9189(4) | 1.8819(4) |
| (O) - ($Fe^B$) | 2.0576(8) | 2.1142(13) | 2.0324(7) | 2.0509(7) |
| (O) - ($Ce^B$) | - | 2.1142(13) | 2.0324(7) | 2.0509(7) |
| (O) - ($Ni^B$) | 2.1099(8) | 2.1142(13) | 2.0324(7) | 2.0509(7) |
| (O) - ($Zn^A$) | 1.8683(5) | 1.7835(6) | 1.9189(4) | 1.8819(4) |
| ($Fe^B$) - ($Ni^B$) | 2.7620(5) | 2.9639(13) | 2.9589(8) | 2.9572(8) |
| ($Ni^B$) - ($Ce^B$) | - | 2.9639(13) | 2.9589(8) | 2.9572(8) |

**Table 4**
Oxygen anions positional parameter ($u$), hopping length ($L_A$) and ($L_B$) of charge carriers between A and B sites, Ionic packing coefficient ($P_A$), ($P_B$), degree of ionic packing ($\alpha$), and tolerance factor ($T$) for S1–S4 samples.

| Samples | $u$ | $L_A$ (Å) | $L_B$ (Å) | $P_A$ | $P_B$ | $\alpha$ | $T$ |
|---|---|---|---|---|---|---|---|
| S1 | 0.2540(2) | 3.6208(8) | 2.9564(8) | 0.2935 | 0.3585 | 0.5827 | 1.0237 |
| S2 | 0.2558(2) | 3.6300(5) | 2.9639(5) | 0.2919 | 0.3757 | 0.5861 | 0.9887 |
| S3 | 0.2574(2) | 3.6218(3) | 2.9572(3) | 0.2686 | 0.3564 | 0.5817 | 1.0258 |
| S4 | 0.2549(2) | 3.6239(2) | 2.9589(2) | 0.2121 | 0.3505 | 0.5841 | 1.0315 |

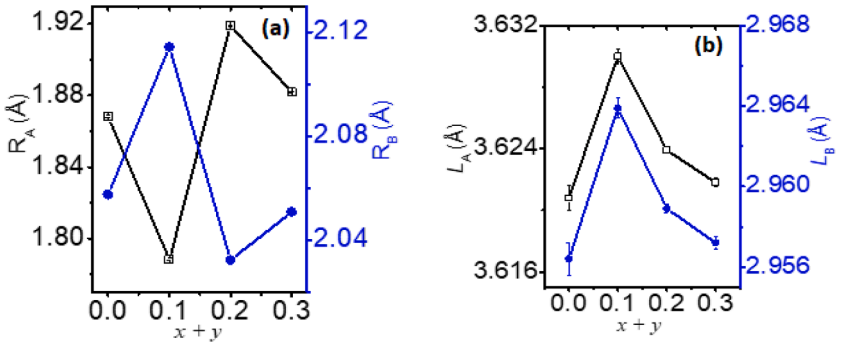


**Fig. 4.** . (a) Average bond lengths $R_A$ and $R_B$ for A and B sites respectively for S1–S4 samples. (b) The magnetic ion hopping lengths ($L_A$) and ($L_B$ ) for A and B sites respectively for S1–S4 samples.

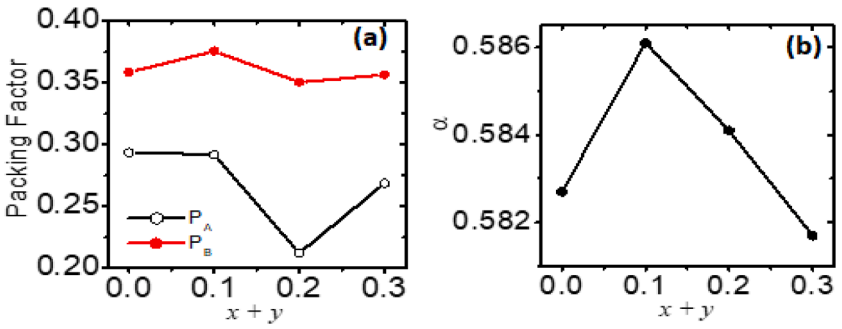


**Fig. 5.** (a) Packing factor$P_A$ and $P_B$for A and B sites respectively for S1–S4 samples. (b) Variation of fulfillment coefficient $\alpha$with S1–S4 samples.

**Table 5**
Estimated cation distribution based on atomic site occupation for samples.

| Sample | Tetrahedral A- sites | Octahedral B-sites |
|---|---|---|
| S1 | $Zn_{0.418}Fe_{0.519}$ | $Zn_{0.119}Ni_{0.4}Fe_{1.481}$ |
| S2 | $Zn_{0.439}Ni_{0.032}Fe_{0.529}$ | $Zn_{0.161}Ni_{0.368}Ce_{0.1}Fe_{1.371}$ |
| S3 | $Zn_{0.473}Ni_{0.111}Fe_{0.416}$ | $Zn_{0.027}Ni_{0.389}Ce_{0.1}Fe_{1.484}$ |
| S4 | $Zn_{0.307}Ni_{0.104}Fe_{0.589}$ | $Zn_{0.093}Ni_{0.496}Ce_{0.1}Fe_{1.311}$ |

plotted in Fig. 3(b) provides some insight into the degree of distortion of the spinel lattice. Depending on the centre of symmetry, the ideal values of $u$ are 0.250 with the origin taken at the octahedral B-site and 0.375 if the centre of symmetry is at the tetrahedral A-site [44]. The centre of symmetry for the reported samples here was taken to be at the octahedral site. In general, $u > 0.250$ for most materials reported in literature [44,45]. This is consistent with the present set of values in Table 4.

The structural factors $T$ in Table 4 were estimated using the equation

$$T = \frac{1}{\sqrt{3}}\left(\frac{r_A + R_0}{r_B + R_0}\right) + \frac{1}{\sqrt{2}}\left(\frac{R_0}{r_A + R_0}\right) \quad (2)$$

where $R_0$ is radius of the oxygen ions (1.38 Å) [33,34] while $r_A$ and $r_B$ are the ionic radii at the tetrahedral site and octahedral site respectively. The values of $T$ are very close to unity for all samples which indicate minor presence of defects.

The values of the fulfilment coefficient $\alpha$ and packing ionic coefficients $P_i$ (where $i = A,B$) in Table 4 are all less than 1. This indicates some presence of cation/anion vacancies on both tetrahedral and octahedral sites [35,36]. The compositional dependences are shown in Fig. 5 (a) and (b) for $P_i$ and $\alpha$ respectively. $P_A$ decreases more significantly than $P_B$ to indicate dominant $Zn^{2+}$ vacancies at the tetrahedral A sites [45]. The variation of the fulfilment coefficient of the unit cell in the range 0.582–0.585 appears to confirm mixed inverse-normal spinel phases [45]. The cation distribution shown in Table 5 was estimated from the site occupancy ($g$) of individual atoms.

The starting model assumed all Zn ions in the A sites and a fraction of Fe ions in the A and B sites, Ni and Ce ions all occupied the B sites [37]. The atomic coordination ($x_i = y_i = z_i$) and their respective $g$ values are recorded in Table 6. To distribute the cations accordingly, the distribution was constrained to preserve the stoichiometric compositions of the samples (i.e., $A_1B_2O_4$). As expected, most $Zn^{2+}$ ions occupy the A sites whilst minor $Zn^{2+}$ ions are observed on the B sites. Furthermore, $Ni^{2+}$ inversion was also observed with the introduction of $Ce^{3+}$ ions on the B sites. The inversion is attributed to the nano-particle nature of the synthesized samples.

HRTEM images and particle size distributions for the samples are presented in Fig. 6. The shapes of the nanoparticles range from semi-spherical to spherical shapes, and are semi-uniformly dispersed. Some of the nanoparticles were agglomerated which could be ascribed to magnetic interactions and presence of weakly interacting van der Waals interactions [46]. The average particle sizes obtained from HRTEM

**Table 6**
Atomic coordination ($x_i, y_i, z_i$) and occupancy ($g$) for the reported samples.

| Atom | S1 $x_i = y_i = z_i$ | $g$ | S2 $x_i = y_i = z_i$ | $g$ | S3 $x_i = y_i = z_i$ | $g$ | S4 $x_i = y_i = z_i$ | $g$ |
|---|---|---|---|---|---|---|---|---|
| $Fe^A$ | 0.125 | 0.519 | 0.125 | 0.529 | 0.125 | 0.416 | 0.125 | 0.589 |
| $Zn^A$ | 0.125 | 0.481 | 0.125 | 0.439 | 0.125 | 0.473 | 0.125 | 0.307 |
| $Ni^B$ | 0.500 | 0.400 | 0.500 | 0.368 | 0.500 | 0.389 | 0.500 | 0.496 |
| $Ce^B$ | - | - | 0.500 | 0.100 | 0.500 | 0.100 | 0.500 | 0.100 |
| $Fe^B$ | 0.500 | 1.481 | 0.500 | 1.371 | 0.500 | 1.484 | 0.500 | 1.311 |

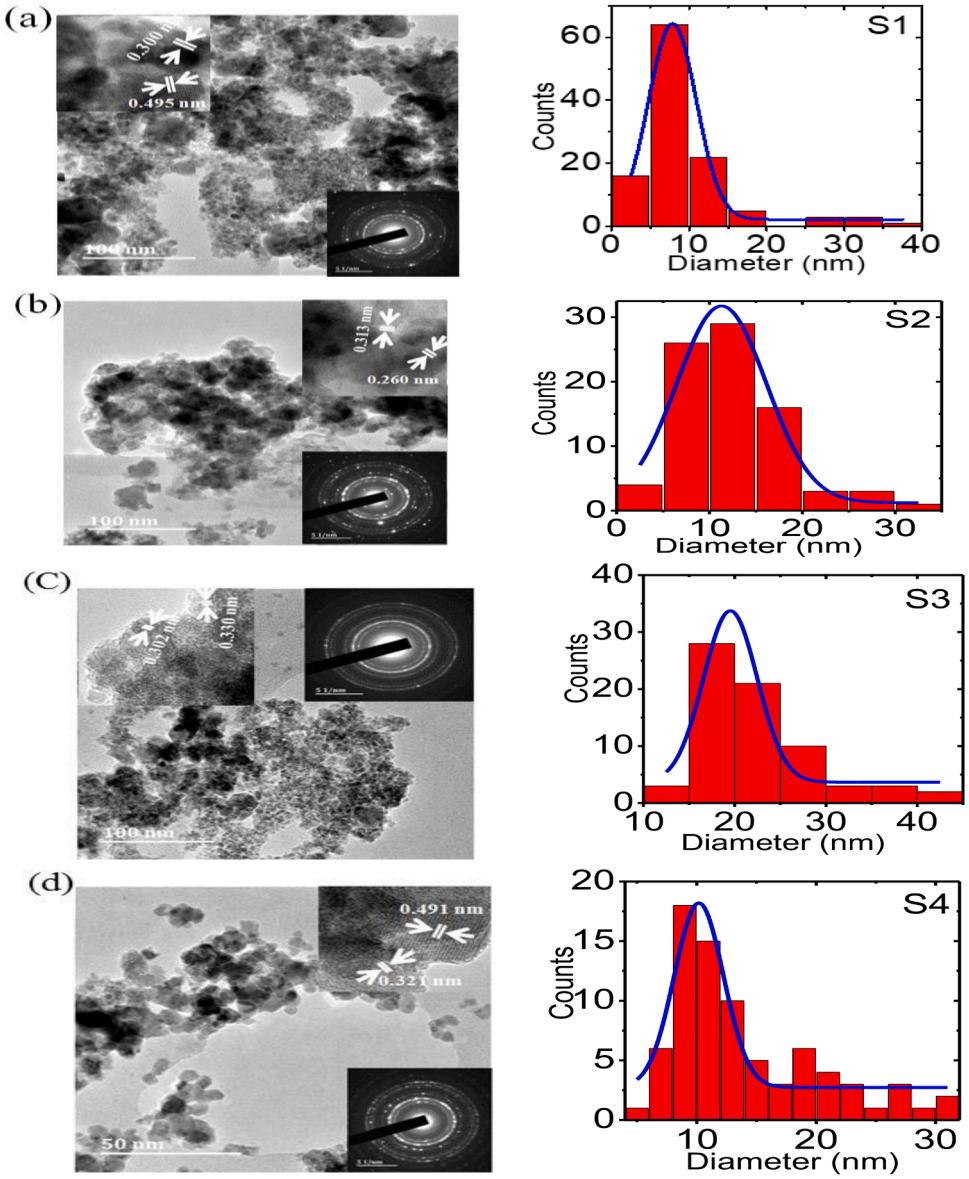


**Fig. 6.** HRTEM micrographs of S1 (a), S2 (b), S3 (c), and S4 (d) samples and their corresponding particle size distributions.

micrographs using ImageJ software [47] are tabulated in Table 2 also presented in Fig. 3(a). The concentric circles of the diffraction patterns in the insets of Fig. 6 indicate the polycrystalline nature of the nanoparticles with well-resolved lattice fringes which for *d* values near 0.300, 0.495, 0.330 and 0.260 nm correspond to lattice planes {220}, {111}, {311} and {400} respectively. SEM micrographs of as-synthesized ferrite samples in Fig. 7 show monodispersed, semi-spherical, and aggregates that further substantiate the HRTEM results.

BETand BJH measurements were conducted in order to determine the specific surface area (SSA) and pore-size distribution. Fig. 8 show results of typical measurements for sample S3. In fact, all samples exhibited similar IV isotherms with H1-type pressure hysteresis loops at relatively low pressures. This resembles the mesoporous MCM-41 material with homogenous pore distribution. The inset insert in Fig. 8 shows the average pore size that contributes dominantly to pore volume. The SSAs and average pore sizes are listed in Table 7. These parameters have significant effect on gas sensing properties. Large surface area leads to enhanced reaction between oxygen species and detected gas molecules [40]. In addition, porous materials have also been shown to be effective at enhancing gas sensing abilities [41].

### 3.2. *Raman spectroscopy results*

Raman spectroscopy is a sensitive tool that can be used to investigate structural configurations and transitions, lattice dynamics, and cation distribution for spinel ferrites. This owes to its spatial resolution to explore atomic vibrations for materials that exhibit Raman active vibrational modes. The Rietveld refinement results confirmed mixed cubic spinel structure belonging to $Fd\bar{3}m$ space group consisting of two A-B sublattices having 56 atoms in a complete unit cell and 14 atoms in the smallest Bravais cell. This indicates that there are 42 possible vibration optical modes [37,42]. Room temperature Raman spectra for the reported samples are shown in Fig. 9. The spectra were excited by a 514 nm line of coherent Innova 99 $Ar^{+}$ - ion laser with exposure time of 10 s at 10 % laser power of 150 mW maximum.

To individualize peaks in the spectra, the Raman spectra were further de-convolved via least squares minimization method of Lorentzian functions corresponding to the$E_g$, $T_{2g}$ and $A_{1g}$ peaks in the spectra. At ambient conditions, it is well known that there are five Raman active modes ($A_{1g} + E_g + 3T_{2g}$) for spinel ferrites [48,49]. These modes have been reported to be associated with the vibration of oxygen and metal

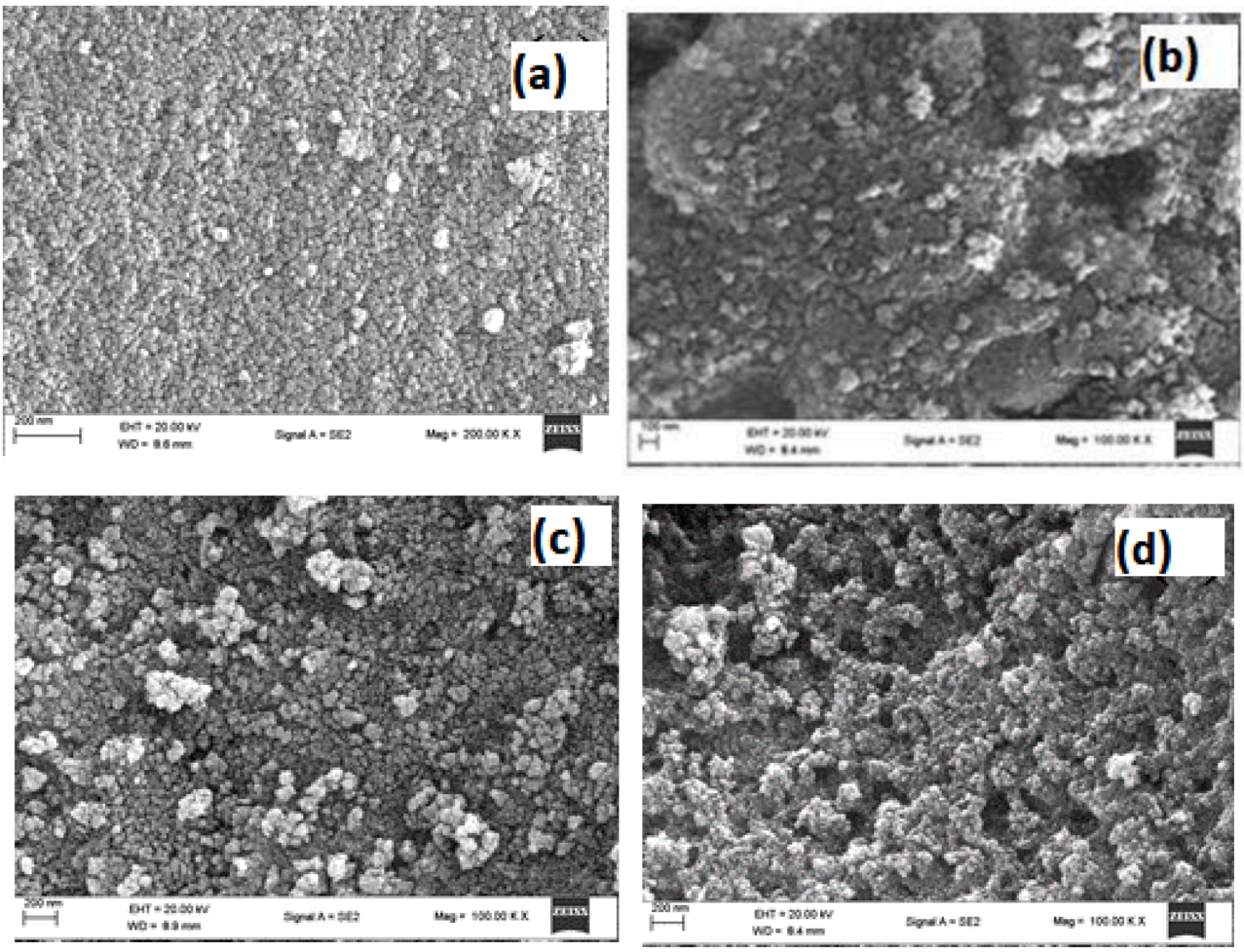


**Fig. 7.** SEM images for prepared S1(a), S2(b), S3(c), and S4(d) samples.

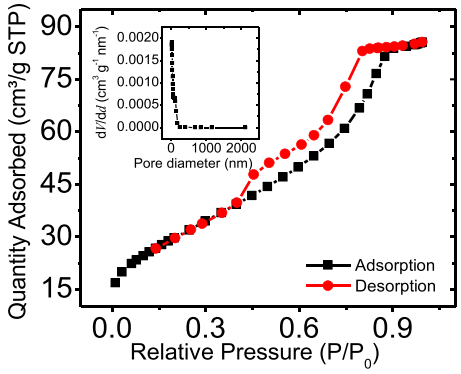


**Fig. 8.** $N_2$ adsorption-desorption BET isotherms with BHJ pore size distribution inset for sample S3.

**Table 7**
Specific surface area (SSA) and average pore size distribution for the report samples.

| Comp. | SSA ($m^2g^{-1}$) | Pore size (nm) |
|---|---|---|
| S1 | 64 | 115 |
| S2 | 73 | 126 |
| S3 | 58 | 120 |
| S4 | 108 | 48 |

ions at A and B sites [48,50]. In the frequency range 200–800 $cm^{-1}$, three distinct first order Raman active modes are observed and attributed to $E_g$, $T_{2g}$ and $A_{1g}$whose peak frequencies are listed in Table 8. These first-order Raman modes are closely matched to those reported in the literature for similar materials [38]. This further confirms the formation of single-phase spinel ferrites in the present set of samples. The relatively low-frequency Raman mode $E_g$ is related to vibrations occurring at the octahedral $BO_6$ sites attributed to the symmetric bending of oxygen ions with metal ions located at the octahedral sites. The $T_{2g}$ Raman mode can be associated with the asymmetric or symmetric stretching vibration of oxygen ions and metals at octahedral or tetrahedral sites. The high-frequency Raman vibration mode $A_{1g}$ is associated with symmetric stretching of oxygen ions with metal ions at the tetrahedral $AO_4$ site sub-lattice. The observed line broadening in Raman modes is probably due to lack of long-range crystalline order expected for nanoparticles or may arise from the statistical cation distribution at the A and B site sub-lattice. The variation of the frequencies with Ce and Ni substitutions of the active modes $E_g$, $T_{2g}$ and $A_{1g}$ could be related to changes in chemical bond lengths given in Table 3.

### 3.3. Magnetization measurements

Magnetic interactions in ferrites are mediated by oxygen anions and occur via super-exchange interactions [24,51,52]. These interactions play a vital role in determining the overall strength of the magnetic interactions (A-A, A-B, B-B) and the effective magnetization of a sample. We investigate the effects of $Ce^{3+}$ doping and varying $Zn^{2+}$ and $Ni^{2+}$ contents. The magnetizations of the samples in response to applied fields

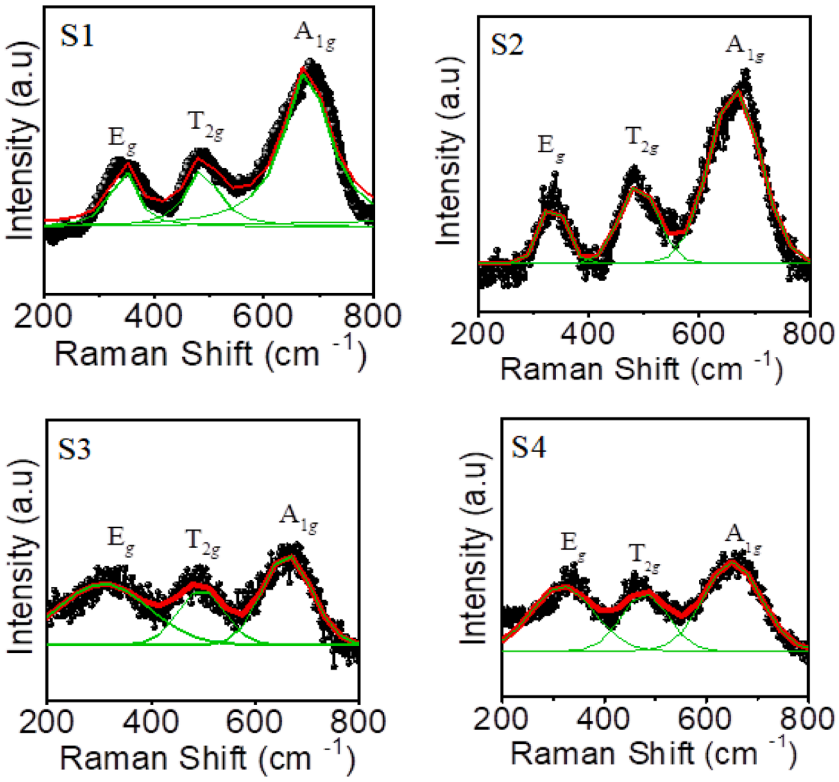


**Fig. 9.** Raman spectra for as-prepared S1–S4 samples.

**Table 8**
Peak positions of Raman active modes.

| Sample | $E_g$(cm$^{-1}$) | $T_{2g}$(cm$^{-1}$) | $A_{1g}$(cm$^{-1}$) |
|---|---|---|---|
| S1 | 344 | 492 | 677 |
| S2 | 335 | 490 | 664 |
| S3 | 308 | 496 | 661 |
| S4 | 318 | 479 | 650 |

at room temperature are given in Fig. 10(a). All samples were subjected to a field sweeps of up to ±20 kOe. Fig. 10(b) show the initial magnetization curves from which the initial susceptibility ($\chi_0$), high field susceptibility ($\chi$ ) and saturation magnetization ($M_S$) can be obtained. The fits to the high field initial magnetization data are based on the empirical formula for the law of approach to saturation given by

$$M = M_S\left(1 - \frac{a}{H} - \frac{b}{H^2}\right) + \chi H \tag{3}$$

where $a$ and $b$ are constants that depend on defects and magneto-

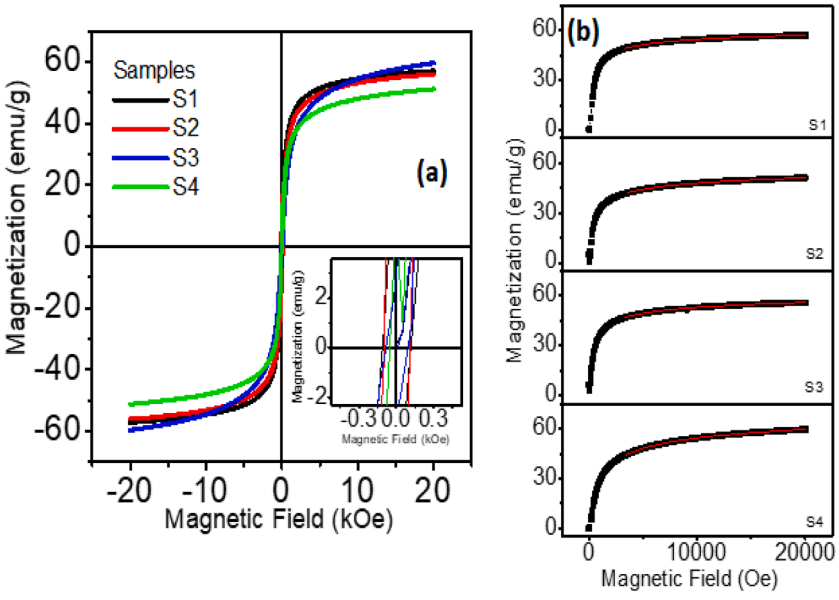


**Fig. 10.** (a) Room temperature hysteresis loops for samples S1–S4. (b) Initial magnetization curves fitted at high applied fields.

**Table 9**
Saturation magnetization ($M_S$), coercivity ($H_C$), remnant magnetization ($M_R$), squareness ratio ($M_R/M_S$), magnetic anisotropy constant ($K_{eff}$), initial magnetic susceptibility ( $\chi_0$ ) and effective magnetic moments ( $\mu_{eff}$).

| Comp. | $M_S$ (emu/g) ±0.1 | $H_C$ (Oe) ±2 | $M_R$(emu/g) ±0.01 | $MR/MS$ ±0.001 | *Keff* (emu.g−1Oe−1) | χ2 (emu g−1Oe−1) | $(\mu_{eff})_B - (\mu_{eff})_A(\mu_B)$ |
|---|---|---|---|---|---|---|---|
| S1 | 57.01 | 114 | 9.12 | 0.16 | 6598 | 0.0762 | 6.83 |
| S2 | 56.06 | 105 | 12.08 | 0.22 | 5976 | 0.0581 | 6.22 |
| S3 | 59.67 | 89 | 3.03 | 0.05 | 5392 | 0.0369 | 7.39 |
| S4 | 50.92 | 53 | 5.29 | 0.10 | 2740 | 0.0561 | 5.67 |

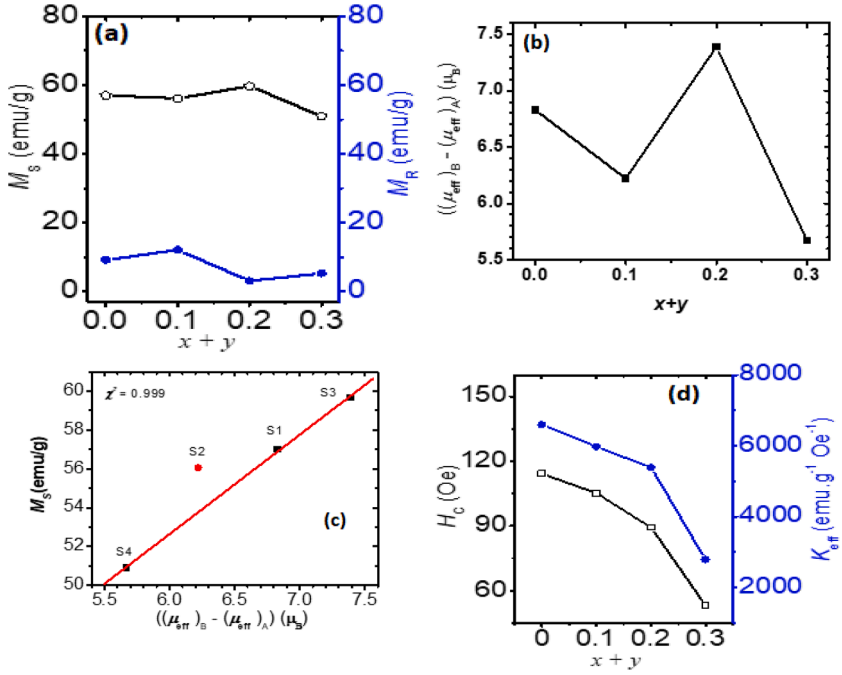


**Fig. 11.** (a) Relation of $M_S$ and $M_R$ with compositions, $x+y$. (b) Variation of effective magnetic moments with composition, $x+y$. (c) Correlation between $M_S$ and effective magnetic moments. (d) Changes in coercivity, $H_C$ and anisotropy constant, $K_{eff}$ with composition.

crystalline anisotropy, respectively [44]. The hysteresis loops are almost symmetrical about the zero-field axis for all the samples (see inset: Fig. 10). Several factors alter the magnetic properties of a material. These include cation distribution, grain size, chemical components, crystal structure, vacancy and defect concentration, and internal stresses. The narrow magnetic hysteresis loops indicate soft magnetic nature of these materials. The $M-H$ curves vary with Ce doping and stoichiometry of Ni, Zn or Fe contents at A and B sites. The results of the analyses of the initial magnetization curves and hysteresis loops are given in Table 9. These include initial susceptibilities, saturation magnetizations, coercive fields and remnant magnetizations. In spinel ferrites, the net magnetization is the vector sum of the net effective magnetic moments of cations at the A and B sites. The saturation magnetizations can be expressed as [45,53]

$$M_S = |M_B - M_A|. \tag{4}$$

We may therefore assume that were $(\mu_{eff})_i$ for $i = \mathrm{A,B}$ are effective magnetic moments

$$M_S \propto \left| (\mu_{eff})_B - (\mu_{eff})_A \right| \tag{5}$$

which can be deduced from the estimated cation distributions in Table 5. The net effective moments are also presented in Table 9 for the current set of samples. The values of $M_S$ in Fig. 11(a) can therefore be attributed to A and B site occupancy by cations with associated magnetic moments: $Zn^{2+}$ (0 $\mu_B$), $Ni^{2+}$ (2.83 $\mu_B$), $Fe^{3+}$ (5.92 $\mu_B$) and $Ce^{3+}$ (2.54 $\mu_B$) [54,55].

The changes in $M_S$ with composition, $x+y$ in Fig. 11(a) appear to be similar to that of $(\mu_{eff})_B - (\mu_{eff})_A$ in Fig. 11(b). This is confirmed further by a linear correlation between $M_S$ and $(\mu_{eff})_B - (\mu_{eff})_A$ in Fig. 11(c) which can justify the cation distributions in Table 5 to be reliable. The correlation is best if sample S2 is excluded from the fit to reflect increased Ni content between samples S1, S3 and S4. The remnant magnetizations $M_R$ for all the samples are small (see Table 9 and Fig. 11 (a)) with the squareness ratio $M_R/M_S$ less than 0.5. This suggests that all the samples S1 to S4 consist of single magnetic domain nanoparticles [56]. Fig. 11(d) shows the values of the coercive fields, $H_C$ deduced from the hysteresis loops and the calculated values of the effective magneto-anisotropy constants, $K_{eff}$ using the Stoner-Wohlfarth random anisotropy formula [46,47,57] where

$$H_C = \frac{0.985 K_{eff}}{M_S}. \tag{6}$$

Coercive fields can provide useful information about the microstructure, magnetic reversal processes and internal stresses in the synthesized compounds. Fig. 11(d) shows that both $H_C$ and $K_{eff}$reduce significantly with Ce and Ni substitutions for compositions, $x+y$. This is typical of Ni ferrite samples to be associated with soft magnetic properties. For samples that contain magnetic nanoparticles, the magnetization responses as a function of applied magnetic fields can provide some useful information about structural changes. This may occur due to possible phase changes of the nanoparticles and associated crystallite sizes. Typical measurements involve $M-H$ curves and significant

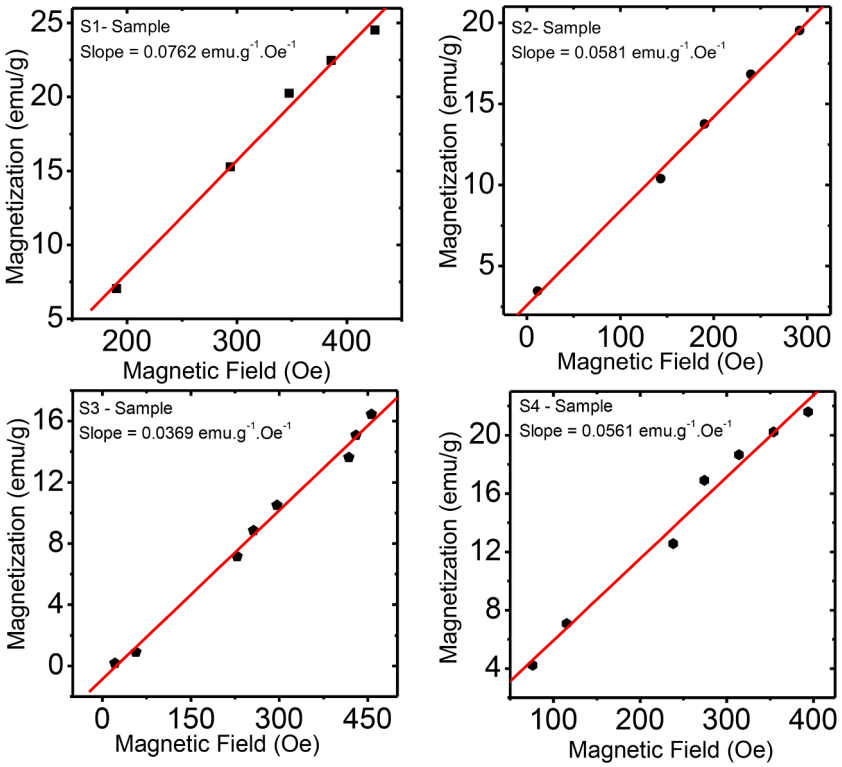


**Fig. 12.** Low field initial magnetization curves. The slopes are proportional to the initial susceptibilities ($\chi_0$).

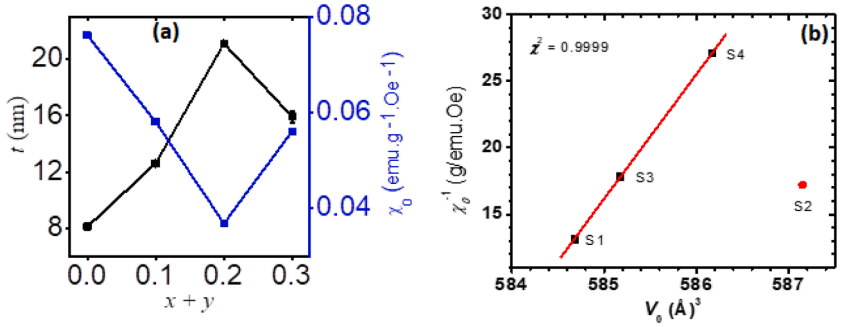


**Fig. 13.** (a) Crystallite sizes and initial susceptibilities for samples S1–S4. (b) Correlation between the inverse susceptibility, $\chi_0$ with unit cell volume, $V_0$.

changes in the slopes associated with hysteresis loops and initial magnetization curves have been observed [48,49,58,59] which show significant changes in the slopes of $M-H$ curves that can be associated with initial susceptibilities.

Fig. 12 shows the low field initial magnetization curves for the current set of samples (S1 to S4) which exhibit good linear fits to the data with slopes that are proportional to the initial susceptibilities ($\chi_0$). Fig. 13(a) shows significant changes in the slopes (or $\chi_0$) with composition which vary similarly to crystallite sizes but inverted. Following similar studies [58,59], we can assume a reciprocal relationship between $\chi_0$ and unit cell volumes $V_0$ (from Table 2). Hence,

$$\chi_0^{-1} \propto V_0. \tag{7}$$

A very strong linear relationship between $\chi_0^{-1}$ and $V_0$ is clearly confirmed in Fig. 13(b) for samples S1, S3 and S4 which appear to be sensitive to $Ni^{2+}$ ion content and yet again confirming the general nature of such a correlation.

### 3.4. Mössbauer spectroscopy

The $^{57}$Fe Mössbauer spectra are shown in Fig. 14. These were fitted by paramagnetic doublets ($D$) and sextets. The doublets are associated with magnetically disordered local spins of Fe ions that can also be attributed to superparamagnetic nanoparticles. The sextets account for the fraction of Fe ions that are in magnetically ordered states. The spectra were fitted using Recoil software via the Lorentzian line shapes with fit parameters listed in Table 10. All measurements were performed at room temperature (about 300 K) relative to a 25 μm thick high purity alpha iron foil, used for velocity calibration. The isomer shift values ($0.32 \pm 0.04$ mm/s) obtained are all consistent with the presence of $Fe^{3+}$ ions [50]. Fig. 15 shows the changes in hyperfine fields at octahedral B sites with composition $x+y$. The trend is similar to that observed for $M_S$ in Fig. 11(a) where the B site moments make dominant contributions. The hyperfine fields are attributed to super-exchange interactions between atomic magnetic moments and their increase at B site can also be associated with increased particle sizes [60]. In spinel ferrites, the random arrangement of cations at the tetrahedral A sites affects the hyperfine fields at B sites and vice-versa with the B sites being more

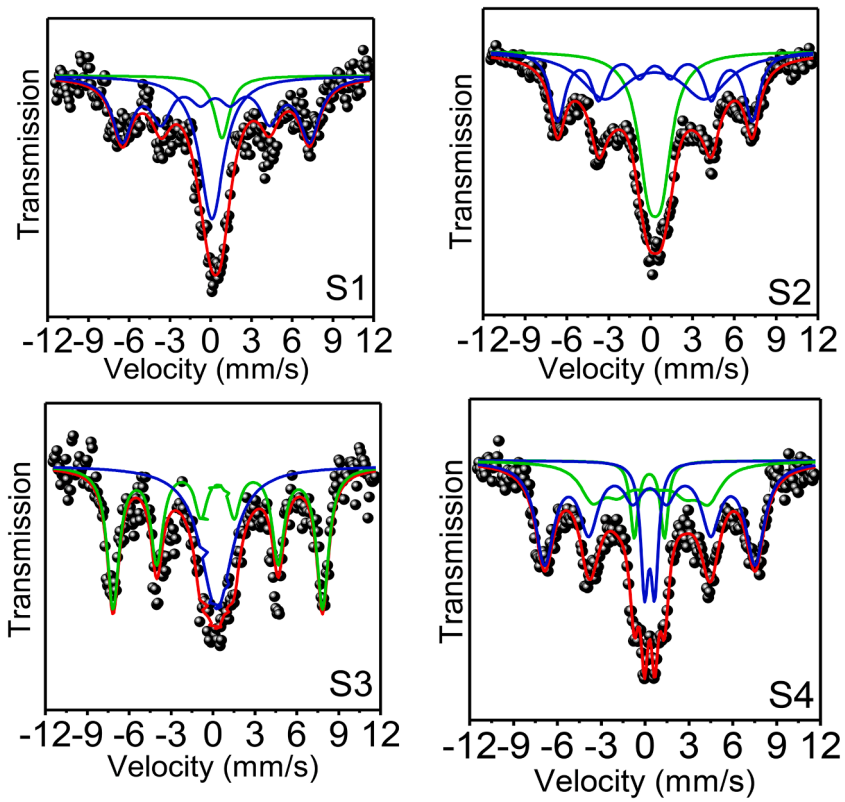


**Fig. 14.** Fitted Mössbauer spectra of samples S1–S4.

**Table 10**
Variation of isomer shifts ($I_S$), Quadrupole split ($Q_S$), Line width (L), Hyperfine fields ($H_f$), and fractional Fe ions population ($f$(%)) for the reported nano ferrites compounds.

| Comp. | Sites | $I_S$(mm/s) ±0.01 | $Q_S$ (mm/s) ±0.01 | $L$ (mm/s) ±0.02 | $H_f$ (kOe) ±10 | $f$(%)±0.5 | $\chi^2$ |
|---|---|---|---|---|---|---|---|
| S1 | $D_A$ | 0.32 | 2.01 | 0.98 | – | 15 | 0.89 |
| | $D_B$ | 0.31 | 0.84 | 0.83 | – | 35 | |
| | $B$ | 0.35 | 0.02 | 0.89 | 435 | 50 | |
| S2 | $D_A$ | 0.32 | 0.94 | 0.90 | – | 35 | 0.83 |
| | $D_B$ | 0.30 | 2.23 | 2.02 | – | 33 | |
| | $B$ | 0.32 | -0.04 | 0.65 | 432 | 32 | |
| S3 | $A$ | 0.27 | 0.04 | 0.56 | 238 | 40 | 0.85 |
| | $B$ | 0.34 | 0.24 | 1.13 | 465 | 60 | |
| S4 | $D_A$ | 0.29 | 2.04 | 0.32 | – | 09 | 0.83 |
| | $D_B$ | 0.31 | 0.69 | 0.31 | – | 12 | |
| | $A$ | 0.42 | -0.04 | 1.02 | 246 | 25 | |
| | $B$ | 0.33 | -0.05 | 0.77 | 446 | 54 | |

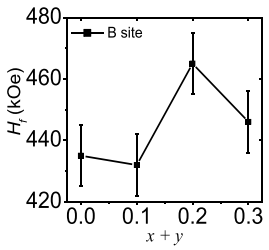


**Fig. 15.** Changes in hyperfine field at B sites for samples S1–S4.

affected by the changes in cation distributions [61,62].

The Mössbauer spectra become more magnetically ordered for samples S3 and S4 with higher hyperfine fields at the B sites. This suggests that the distribution of $Zn^{2+}$ and $Ni^{2+}$ ions influence the magnetic order. There is initially a slight reduced hyperfine field ($H_f$), when lower moment $Ce^{3+}$ replaces $Fe^{3+}$ ions for S2. This is followed by increased magnetic order when nonmagnetic $Zn^{2+}$ ions are replaced by magnetic $Ni^{2+}$ ions which lead to higher saturation magnetizations and higher hyperfine fields for samples S3 and S4. The quadruple splitting values in Table 10 vary significantly which indicate high asymmetry at both sites A and B.

### 3.5. Gas sensing perperties

The gas sensing responses of the samples were investigated for reducing gases $SO_2$ and CO. The adsorption of the oxygen species on the sample surfaces has been shown to be proportional to the gas sensing characteristics [63] and the chemisorbed oxygen species influence the surface conductivity. The response of a sensor is also known to depend on several factors such as morphology, structure, specific surface area (SSA) of the particles, synthesis technique and elemental composition of the compound. Figs. 16 and 17 show electrical responses with increasing gas concentration. As expected, the current increased with increasing gas concentration. The responses were obtained at activation temperatures of 100 °C and 150 °C. The sensing mechanism is still widely contested. However, for the detection of reducing gases $SO_2$ and CO can be explained using the electron depletion theory [64]. The exposure of a sensor materials in air results in the adsorption of oxygen molecules on the sensor surface leading to the extraction of electrons from sensor material surface to form oxygen ions such as $O_2^-$, $O^-$, and $O^{2-}$ depending on the temperature [65]. Based on the reported activation temperatures [65], the type of oxygen ions adsorbed on these sensor surfaces after capturing an electron is most likely $O_2^-$. The equations representing the reactions at the sensor surface for $SO_2$ and CO gases can therefore be

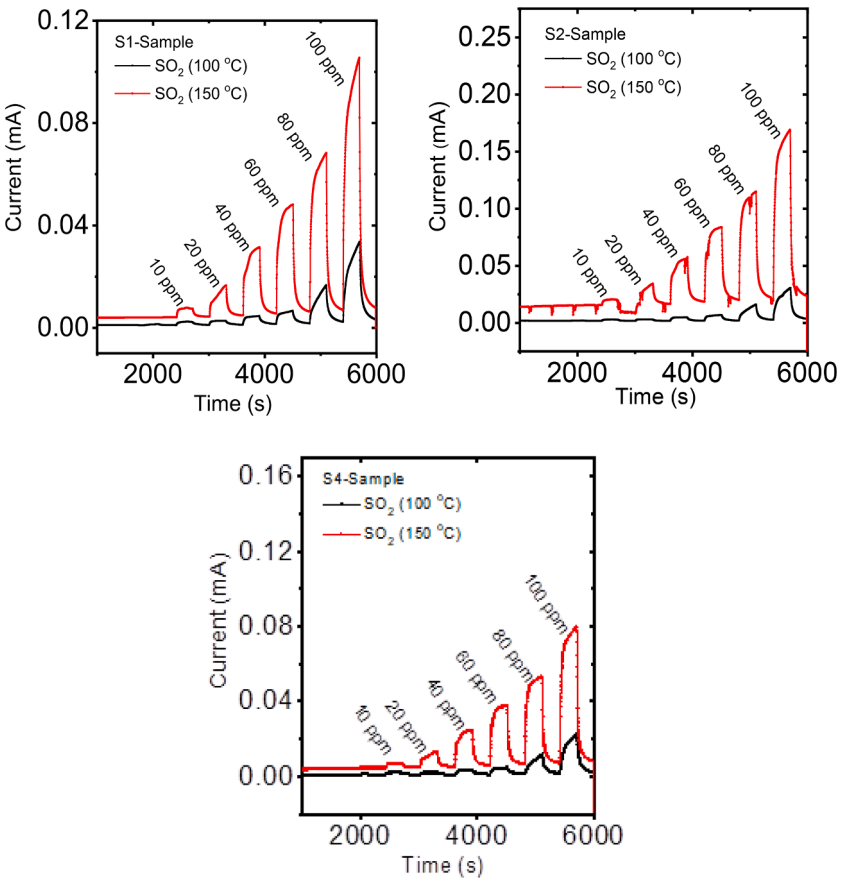


**Fig. 16.** $SO_2$ dynamic response at 100 °C and 150 °C for samples S1, S2, and S4.

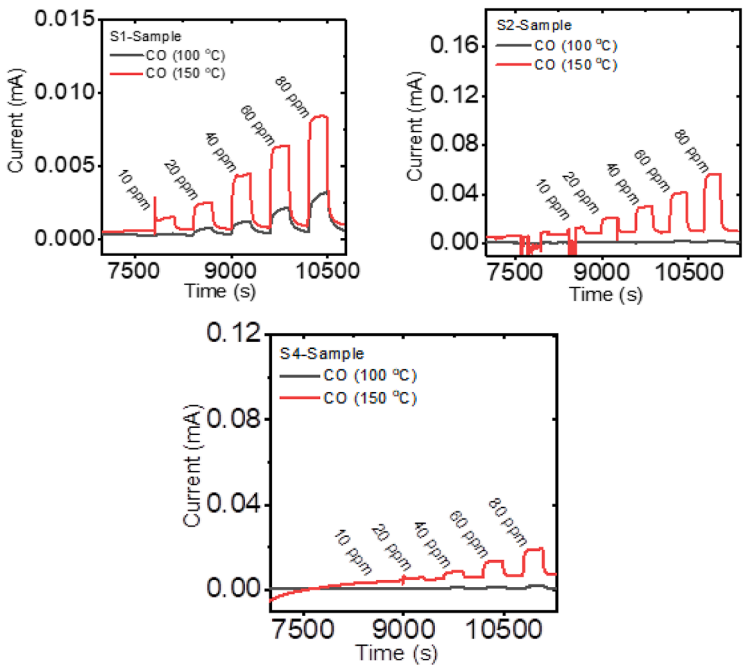


**Fig. 17.** CO dynamic response at 100 °C and 150 °C for samples S1, S2, and S4.

assumed to be as follows:

$$O_2\ (gas) \rightarrow O_2\ (ads) \quad (8)$$

$$O_2\ (gas) + e^- \rightarrow O_2^-\ (ads) \quad (9)$$

$$2SO_2\ (gas) + O_2^-\ (ads) \rightarrow 2SO_3\ (gas) + e^- \quad (10)$$

$$2CO\ (gas) + O_2^-\ (ads) \rightarrow 2CO_2\ (gas) + e^- \quad (11)$$

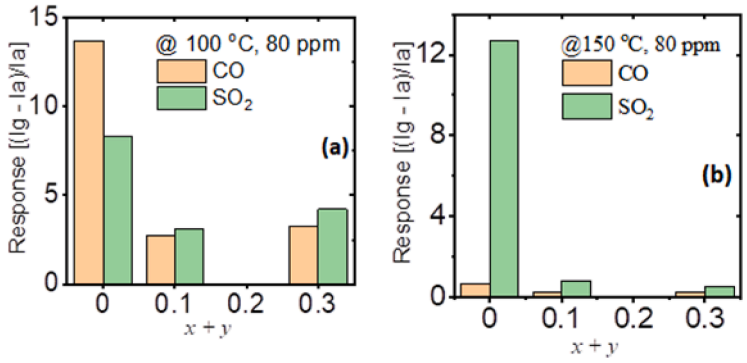


**Fig. 18.** (a) $SO_2$ and CO response at 100 °C for samples S1, S2, and S4. (b) $SO_2$ and CO response at 150 °C for samples S1, S2, and S4.

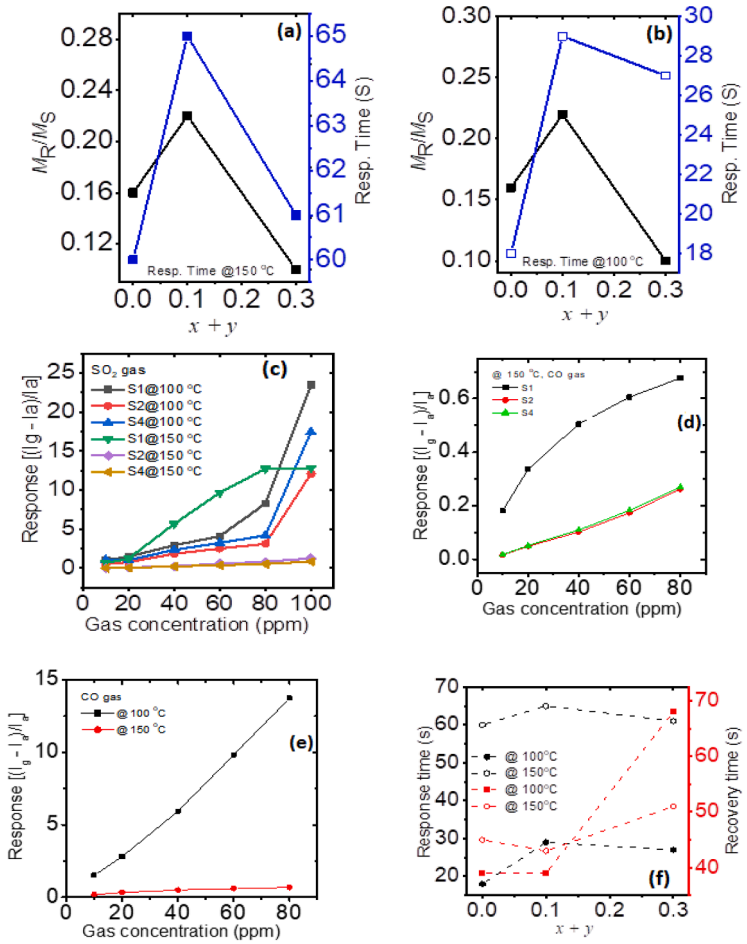


**Fig. 19.** (a) Relation between squareness ratio verses response time for $SO_2$ at 100 °C. (b) Relation between squareness ratio verses response time for $SO_2$ at 150 °C. (c) $SO_2$ response at 100 °C and 150 °C for samples S1, S2, and S4 for varying gas concentrations. (d) CO response at 150 °C for samples S1, S2, and S4 for varying gas concentrations. (e) CO response at 100 °C and 150 °C for sample S1 for varying gas concentrations. (f) $SO_2$ response and recovery times at 100 °C and 150 °C for samples S1, S2, and S4 at 80 ppm.

Both $SO_2$ and CO gases are more reducible than $O_2$. Hence, when the $O_2$ is exposed to $SO_2$ and CO, their reaction releases more electrons at the surfaces of the sensors and forms unstable $SO_3$ and $CO_2$. This results in reduced thickness of the electron depletion layers and increases conductivity. The sensing responses can be calculated using the formula

$$\text{Resp} = \frac{I_g - I_a}{I_a} \tag{12}$$

where $I_a$ is the current through the sensor in air and $I_g$ is the current in reducing gas [66]. The best response for both $SO_2$ and CO was found for S1 sensor material. The highest response values of 14.7 at 100 °C and 13.7 at 150 °C were obtained at concentrations of 80 ppm as shown in Fig. 18(a) and (b).

The sensing responses decrease from S1 to S4. Some of the important factors that affect the electron transfer and gas sensing response are activation energy, adsorbed oxygen quantity and the number of active sites. Hence, the reduction in sensitivity aside from morphology is attributed to cation redistribution i.e., the migration of $Ni^{2+}$ from B- to A-sites with the introduction of $Ce^{3+}$ ions leading to a change in the electronic structure at sensor material surface. This results in reducing

$Ni^{2+}$active sites which also reduce sensor responses. For the current samples S1, S2, and S4, gas sensing decreased while ferromagnetic coupling increased. Akande et al. [35] observed similar behaviour in vanadium oxide $V_2O_5$ sensor material when it transformed from paramagnetic to ferromagnetic state after thermal annealing. The $V_2O_5$ sensor material in the paramagnetic state showed a more superior response to $NH_3$ gas compared to ferromagnetic state sensor. This suggests surface spins can affect both gas sensing and magnetic effects. A noteworthy correlation is observed between the squareness ratio $M_R/M_S$ and response times at both 100 °C and 150 °C for $SO_2$ in Fig. 19(a) and (b). Fig. 19(c) shows the responses to $SO_2$ gas concentrations up to 100 ppm for sensors at 100 °C and 150 °C. The response to $SO_2$ for sample S1 at 100 °C shows much improved response of 23.5 at a gas concentration of 100 ppm compared to 18. 8 at 150 °C. Similarly, the responses with respect to CO gas sensing are given in Fig. 19(d) and (e) which also show much higher response at 100 °C especially for the sample S1.

The response and recovery times are also important parameters for gas sensors, defined as the time required for the sensor to reach 90 % saturation response in the presence of a reducing gas and 10 % response in the absence of the gas, respectively. The response and recovery times for the best responding reducing gas $SO_2$ are shown in Fig. 19(f). The lowest response and recovery times were found to be for S1 with times of 18 s and 39 s at 100 °C and 60 s and 45 s at 150 °C respectively.

## 4. Conclusions

Nanocrystalline $Ni_{0.4+x}Zn_{0.6-x}Ce_yFe_{2-y}O_4$materials with a single-phase spinel structure were effectively produced through a modified glycol-thermal method. The results are presented as functions of $x+y$ where $0 \leq x+y \leq 0.3$ associated with samples S1, S2, S3 and S4. The crystallite sizes in the range 8–21 nm obtained from XRD were in agreement with particle sizes obtained from HRTEM. SEM revealed semi-spherical and homogeneously dispersed nanoparticles. The changes in the lattice parameters were found to mirror changes in ionic sizes. The introduction of $Ce^{3+}$ and $Ni^{2+}$ ions altered the cation distribution and influenced changes in magnetic properties. Cation distribution from Rietveld refinement revealed all $Ce^{3+}$ ions occupied the B-sites, whilst $Ni^{2+}$, $Zn^{2+}$, and $Fe^{3+}$ ions occupied both A and B sites confirming formation of mixed spinel ferrites. The changes in saturation magnetizations were found to be consistent with changes in effective magnetic moments and confirm the estimated cation distributions to be reliable. The coercive fields decreased with increased Ni ions normally associated with reduced anisotropy. Significant changes in the initial susceptibilities were observed which show strong correlation between initial susceptibilities with unit cell volumes especially for samples S1, S3 and S4. The magnetic characteristics of synthesized materials makes them useful in high frequency devices and may have potential use as contrast agent in magnetic resonance imaging (MRI). $^{57}Fe$ Mössbauer spectroscopy revealed strengthening of ferromagnetic coupling from S1 to S4 which also appear to be consistent with changes in saturation magnetizations. The studied samples have also been investigated for possible use as gas sensor materials. A correlation between gas sensing response and squareness ratio $\frac{M_r}{M_s}$ was observed. A decrease in the sensing response as the material transition from paramagnetic state to ferromagnetic state. The best sensing characteristics were obtained for the sample$Ni_{0.4}Zn_{0.6}Fe_2O_4$. The sample showed sensitivity preference for $SO_2$ at 100 °C over CO gas. However, at 150 °C, the nano-ferrite showed higher sensitivity for CO gas. For the other samples, the gas sensing responses were much lower.

## CRediT authorship contribution statement

**Sanele T. Dlamini:** Methodology, Formal analysis, Writing – original draft. **Thomas Moyo:** Supervision, Resources, Writing – review & editing. **Amos Nhlapo:** Formal analysis, Writing – review & editing. **Daniel Wamwangi:** Writing – review & editing. **Amos Akande:** Data curation, Writing – review & editing. **Bonex W. Mwakikunga:** Data curation, Writing – review & editing.

## Declaration of competing interest

The authors declare that they have no known competing financial interests or personal relationships that could have appeared to influence the work reported in this paper.

## Data availability

No data was used for the research described in the article.

## Acknowledgments

Sanele Dlamini wishes to thank the research office of the University of KwaZulu-Natal for research support. The University of the Witwatersrand for magnetization measurements and the Council for Scientific and Industrial Research (CSIR), South Africa, for gas sensing measurements.

## References

[1] N. Venkatesh, D.R. Kumar, S. Goud, S.I. Ahmad, P. Veerasomaiah, D. Ravinder, Structural, photocatalytic, electromagnetic properties of rare-earth metal Gd-doped Mg nanoferrites synthesized by citrate gel auto-combustion method, Chem. Pap. 77 (2023) 2749–2767, https://doi.org/10.1007/s11696-023-02664-z.
[2] S.K. Gurav, S.E. Shirsath, R.H. Kadam, D.R. Mane, Low temperature synthesis of $Li_{0.5}Zr_xCo_xFe_{2.5-2x}O_4$ powder and their characterizations, Powder Technol. 235 (2013) 485–492, https://doi.org/10.1016/j.powtec.2012.11.009.
[3] T. Past, Feature 269, Time 80 (1999) 269–280.
[4] K. Kondo, T. Chiba, S. Yamada, Effect of microstructure on magnetic properties of Ni-Zn ferrites, J. Magn. Magn. Mater. 254–255 (2003) 541–543, https://doi.org/10.1016/S0304-8853(02)00859-4.
[5] M.N. Mat, M.K. Halimah, W.M.D.W. Yusoff, H. Mansor, H. Nizam, Y. Zainuddin, T. I.T.M. Aiman, Dielectric and conduction processes and behaviours in $Ni_{0.3}Zn_{0.7}Fe_2O_4$, Mater. Sci. Forum 846 (2016) 311–317, https://doi.org/10.4028/www.scientific.net/MSF.846.311.
[6] M. Atif, Synthesis and temperature dependent magnetic properties of nanocrystalline $Ni_{0.5}Zn_{0.5}Fe_2O_4$ ferrites, Mater. Res. Express 6 (2019), https://doi.org/10.1088/2053-1591/ab121e.
[7] I. Ahmad, T. Abbas, M.U. Islam, A. Maqsood, Study of cation distribution for Cu-Co nanoferrites synthesized by the sol-gel method, Ceram. Int. 39 (2013) 6735–6741, https://doi.org/10.1016/j.ceramint.2013.02.001.
[8] I.H. Gul, W. Ahmed, A. Maqsood, Electrical and magnetic characterization of nanocrystalline Ni-Zn ferrite synthesis by co-precipitation route, J. Magn. Magn. Mater. 320 (2008) 270–275, https://doi.org/10.1016/j.jmmm.2007.05.032.
[9] A.V. Humbe, J.S. Kounsalye, M.V. Shisode, K.M. Jadhav, Rietveld refinement, morphology and superparamagnetism of nanocrystalline $Ni_{0.70-x}Cu_xZn_{0.30}Fe_2O_4$ spinel ferrite, Ceram. Int. 44 (2018) 5466–5472, https://doi.org/10.1016/j.ceramint.2017.12.180.
[10] M. Kaiser, Effect of rare earth elements on the structural, magnetic and electrical behavior of Ni-Zn-Cr nanoferrites, J. Alloy. Compd. 719 (2017) 446–454, https://doi.org/10.1016/j.jallcom.2017.05.155.
[11] O.F. Caltun, L. Spinu, A. Stancu, L.D. Thung, W. Zhou, Study of the microstructure and of the permeability spectra of Ni-Zn-Cu ferrites, J. Magn. Magn. Mater. 242–245 (2002) 160–162, https://doi.org/10.1016/S0304-8853(01)01187-8.
[12] A. Sutka, G. Mezinskis, A. Lusis, D. Jakovlevs, Influence of iron non-stoichiometry on spinel zinc ferrite gas sensing properties, Sens. Actuators B Chem. 171–172 (2012) 204–209, https://doi.org/10.1016/j.snb.2012.03.012.
[13] C. Xiangfeng, J. Dongli, Z. Chenmou, The preparation and gas-sensing properties of $NiFe_2O_4$ nanocubes and nanorods, Sens. Actuators B Chem. 123 (2007) 793–797, https://doi.org/10.1016/j.snb.2006.10.020.
[14] A. Jain, R.K. Baranwal, A. Bharti, Z. Vakil, C.S. Prajapati, Study of Zn-Cu ferrite nanoparticles for LPG sensing, Sci. World J. 2013 (2013), https://doi.org/10.1155/2013/790359.
[15] S.V. Bangale, R.D. Prakshale, S.R. Bamane, Nanostructured $Ni_{0.5}Zn_{0.5}Ce_3O_5$ oxide based electronic nose sensitive to ammonia at operable temperature, Sens. Transducers 139 (2012) 109–121.
[16] F. Tudorache, P.D. Popa, M. Dobromir, F. Iacomi, Studies on the structure and gas sensing properties of nickel-cobalt ferrite thin films prepared by spin coating, Mater. Sci. Eng. B Solid State Mater. Adv. Technol. 178 (2013) 1334–1338, https://doi.org/10.1016/j.mseb.2013.03.019.
[17] T.A. Nhlapo, S.T. Dlamini, T.P. Mokoena, T.C. Mokhena, T.S. Mahule, T.D. Malevu, T. Moyo, Influence of rare-earth elements (RE = Ce, Nd, Gd) on structural, ESR and

Mossbauer spectroscopy studies of $Ni_{0.5}Co_{0.5}RE_{0.03}Fe_{1.97}O_4$ synthesized by M o glycol-thermal method, J. Solid State Chem. 330 (2024) 124479.
[18] G. Frajer, O. Isnard, H. Chazal, G. Delette, Effect of cobalt addition on the magneto-crystalline anisotropy parameter of sintered NiZn ferrites evaluated from magnetization curves, J. Magn. Magn. Mater. 473 (2019) 92–98, https://doi.org/10.1016/j.jmmm.2018.10.030.
[19] D. Nagpal, K.I. Gnanasekar, C.R. Mariappan, A. Kumar, Structural, electrical and gas sensing functionality of fabricated $Co_{1-x}Zn_xFe_{2-x}Ni_xO_4$ (x= 0.0,0.3) nanoparticles, Phys. B Condens. Matter 646 (2022), https://doi.org/10.1016/j.physb.2022.414332.
[20] R. Kashyap, R. Kumar, S. Devi, M. Kumar, S. Tyagi, D. Kumar, Ammonia gas sensing performance of nickel ferrite nanoparticles, Mater. Res. Express 6 (2019), https://doi.org/10.1088/2053-1591/ab55b5.
[21] E. Ranjith Kumar, P. Siva Prasada Reddy, G. Sarala Devi, S. Sathiyaraj, Structural, dielectric and gas sensing behavior of Mn substituted spinel $MFe_2O_4$ (M=Zn, Cu, Ni, and Co) ferrite nanoparticles, J. Magn. Magn. Mater. 398 (2016) 281–288, https://doi.org/10.1016/j.jmmm.2015.09.018.
[22] C. Srinivas, E. Ranjith Kumar, B.V. Tirupanyam, S. Singh Meena, P. Bhatt, C. L. Prajapat, T.V. Chandrasekhar Rao, D.L. Sastry, Study of magnetic behavior in co-precipitated Ni–Zn ferrite nanoparticles and their potential use for gas sensor applications, J. Magn. Magn. Mater. 502 (2020), https://doi.org/10.1016/j.jmmm.2020.166534.
[23] O. Abd-elkader, A.M. Al-enizi, S.F. Shaikh, M. Ubaidullah, M.O. Abdelkader, N. Y. Mostafa, The Structure, Magnetic, and Gas Sensing Characteristics of W-Substituted Co-Ferrite Nanoparticles, Crystals (2022) 1–16, https://doi.org/10.3390/cryst12030393.
[24] S. Joshi, V.B. Kamble, M. Kumar, A.M. Umarji, G. Srivastava, Nickel substitution induced effects on gas sensing properties of cobalt ferrite nanoparticles, J. Alloy. Compd. 654 (2016) 460–466, https://doi.org/10.1016/j.jallcom.2015.09.119.
[25] M. Qayoom, S. Irfan, G.F. Malik, K.A. Shah, M.Q. Lone, R.T.R. Kumar, G.N. Dar, Modified solution combustion-grown Zn-doped Ni–Mg ferrite nanostructures for room temperature NH3 sensing, J. Mater. Sci. Mater. Electron. 33 (2022) 25645–25660, https://doi.org/10.1007/s10854-022-09261-y.
[26] A. Sutka, G. Mezinskis, A. Lusis, M. Stingaciu, Gas sensing properties of Zn-doped p-type nickel ferrite, Sens. Actuators, B Chem. 171–172 (2012) 354–360, https://doi.org/10.1016/j.snb.2012.04.059.
[27] Y. Feng, Y. Wang, D.M. Silevitch, S.E. Cooper, D. Mandrus, P.A. Lee, T. F. Rosenbaum, A continuous metal-insulator transition driven by spin correlations, Nat. Commun. 12 (2021) 1–7, https://doi.org/10.1038/s41467-021-23039-6.
[28] S.K. Nath, M.M. Rahman, S.S. Sikder, M.A. Hakim, S.M. Hoque, Magnetization and magnetic behavior of Ni1-xCdxFe2O4 Ferrites, J. Sci. Technol. 3 (2013) 106–111.
[29] C. Srinivas, E. Ranjith Kumar, B.V. Tirupanyam, S. Singh Meena, P. Bhatt, C. L. Prajapat, T.V. Chandrasekhar Rao, D.L. Sastry, Study of magnetic behavior in co-precipitated Ni–Zn ferrite nanoparticles and their potential use for gas sensor applications, J. Magn. Magn. Mater. 502 (2020) 166534, https://doi.org/10.1016/j.jmmm.2020.166534.
[30] M. Jalaly, M.H. Enayati, F. Karimzadeh, P. Kameli, Mechanosynthesis of nanostructured magnetic Ni-Zn ferrite, Powder Technol. 193 (2009) 150–153, https://doi.org/10.1016/j.powtec.2009.03.008.
[31] T.A. Nhlapo, J.Z. Msomi, T. Moyo, Temperature-dependent magnetic behavior of Mn-Mg spinel ferrites with substituted Co, Ni & Zn, synthesized by hydrothermal method, J. Mol. Struct. 1245 (2021) 131042, https://doi.org/10.1016/j.molstruc.2021.131042.
[32] S. Dlamini, S. Nkosi, T. Moyo, A. Nhlapo, Structural and magnetic characterization of $Co^{2+}$ substituted Ni-Zn ferrite nanoparticles synthesized by refluxing co-precipitation and their potential application as gas sensors, Mater. Sci. Eng. B 294 (2023) 116554, https://doi.org/10.1016/j.mseb.2023.116554.
[33] S.G. Gawas, U.B. Gawas, V.M.S. Verenkar, M.M. Kothawale, R. Pednekar, Structural and magnetic studies of Cu-substituted nanocrystalline Ni–Zn ferrites obtained via hexamine–nitrate combustion route, J. Supercond. Nov. Magn. 30 (2017) 1447–1452, https://doi.org/10.1007/s10948-016-3937-9.
[34] Z. Yan, J. Luo, Effects of Ce[sbnd]Zn co-substitution on structure, magnetic and microwave absorption properties of nickel ferrite nanoparticles, J. Alloy. Compd. 695 (2017) 1185–1195, https://doi.org/10.1016/j.jallcom.2016.08.333.
[35] A.A. Akande, T. Mosuang, C.N.M. Ouma, E.M. Benecha, T. Tesfamicheal, K. Roro, A.G.J. Machatine, B.W. Mwakikunga, Ammonia gas sensing characteristics of $V_2O_5$ nanostructures: a combined experimental and ab initio density functional theory approach, J. Alloy. Compd. 821 (2020), https://doi.org/10.1016/j.jallcom.2019.153565.
[36] G.I. Supelano, A.J. Barón-González, A. Sarmiento Santos, C. Ortíz, J.A. Mejía Gómez, C.A. Parra Vargas, Effect of Mg addition on LaMnO3 ceramic system, J. Mater. Res. Technol. 7 (2018) 77–81, https://doi.org/10.1016/j.jmrt.2017.05.012.
[37] K.E. Sickafus, J.M. Wills, N.W. Grimes, Structure of spinel, J. Am. Ceram. Soc. 82 (1999) 3279–3292, https://doi.org/10.1111/j.1151-2916.1999.tb02241.x.
[38] A. Kumar, P. Sharma, D. Varshney, Structural, vibrational and dielectric study of Ni doped spinel Co ferrites: $Co_{1-x}Ni_xFe_2O_4$ (x=0.0, 0.5, 1.0), Ceram. Int. 40 (2014) 12855–12860, https://doi.org/10.1016/j.ceramint.2014.04.140.
[39] A.A. Birajdar, S.E. Shirsath, R.H. Kadam, S.M. Patange, D.R. Mane, A.R. Shitre, Rietveld structure refinement and cation distribution of substituted nanocrystalline Ni-Zn ferrites, ISRN Ceram. 2012 (2012) 1–5, https://doi.org/10.5402/2012/876123.
[40] L. Kumar, P. Kumar, M. Kar, Cation distribution by Rietveld technique and magnetocrystalline anisotropy of Zn substituted nanocrystalline cobalt ferrite, J. Alloy. Compd. 551 (2013) 72–81, https://doi.org/10.1016/j.jallcom.2012.10.009.
[41] K.A. Mohammed, A.D. Al-Rawas, A.M. Gismelseed, A. Sellai, H.M. Widatallah, A. Yousif, M.E. Elzain, M. Shongwe, Infrared and structural studies of $Mg_{1-x}Zn_xFe_2O_4$ ferrites, Phys. B Condens. Matter 407 (2012) 795–804, https://doi.org/10.1016/j.physb.2011.12.097.
[42] W.B. Dlamini, J.Z. Msomi, T. Moyo, XRD, Mössbauer and magnetic properties of $Mg_xCo_{1-x}Fe_2O_4$ nanoferrites, J. Magn. Magn. Mater. 373 (2015) 78–82, https://doi.org/10.1016/j.jmmm.2014.01.066.
[43] R.D. Shannon, Revised effective ionic radii and systematic studies of interatomic distances in halides and chalcogenides, Acta Crystallogr. Sect. A 32 (1976) 751–767, https://doi.org/10.1107/S0567739476001551.
[44] A.A.H. El-Bassuony, Tuning the structural and magnetic properties on Cu/Cr nanoferrite using different rare-earth ions, J. Mater. Sci. Mater. Electron. 29 (2018) 3259–3269, https://doi.org/10.1007/s10854-017-8261-z.
[45] K.A.M. Khalaf, A.D. Al-Rawas, H.M. Widatallah, K.S. Al-Rashdi, A. Sellai, A. M. Gismelseed, M. Hashim, S.K. Jameel, M.S. Al-Ruqeishi, K.O. Al-Riyami, M. Shongwe, A.H. Al-Rajhi, Influence of Zn2+ ions on the structural and electrical properties of $Mg_{1-x}Zn_xFeCrO_4$ spinels, J. Alloy. Compd. 657 (2016) 733–747, https://doi.org/10.1016/j.jallcom.2015.10.157.
[46] G. Rana, U.C. Johri, A study on structural and magnetic properties of Ni-substituted magnetite nanoparticles, J. Alloy. Compd. 577 (2013) 376–381, https://doi.org/10.1016/j.jallcom.2013.05.184.
[47] C.T. Rueden, J. Schindelin, M.C. Hiner, B.E. DeZonia, A.E. Walter, E.T. Arena, K. W. Eliceiri, ImageJ2: ImageJ for the next generation of scientific image data, BMC Bioinform. 18 (2017) 1–27, https://doi.org/10.1186/s12859-017-1934-z.
[48] R. Nongjai, S. Khan, K. Asokan, H. Ahmed, I. Khan, Magnetic and electrical properties of in doped cobalt ferrite nanoparticles, J. Appl. Phys. 112 (2012), https://doi.org/10.1063/1.4759436.
[49] W.B. White, B.A. DeAngelis, Interpretation of the vibrational spectra of spinels, Spectrochim. Acta Part A Mol. Spectrosc. 23 (1967) 985–995, https://doi.org/10.1016/0584-8539(67)80023-0.
[50] G. Datt, M. Sen Bishwas, M. Manivel Raja, A.C. Abhyankar, Observation of magnetic anomalies in one-step solvothermally synthesized nickel-cobalt ferrite nanoparticles, Nanoscale 8 (2016) 5200–5213, https://doi.org/10.1039/c5nr06791j.
[51] N. Najmoddin, A. Beitollahi, H. Kavas, S. Majid Mohseni, H. Rezaie, J. Åkerman, M. S. Toprak, XRD cation distribution and magnetic properties of mesoporous Zn-substituted $CuFe_2O_4$, Ceram. Int. 40 (2014) 3619–3625, https://doi.org/10.1016/j.ceramint.2013.09.063.
[52] P. Thakur, R. Sharma, M. Kumar, S.C. Katyal, N.S. Negi, N. Thakur, V. Sharma, P. Sharma, Super paramagnetic la doped Mn-Zn nano ferrites: dependence on dopant content and crystallite size, Mater. Res. Express 3 (2016), https://doi.org/10.1088/2053-1591/3/7/075001.
[53] E.E. Ateia, M. Farag, Synthesis of cobalt/calcium nanoferrites with controllable physical properties, Appl. Phys. A Mater. Sci. Process. 125 (2019), https://doi.org/10.1007/s00339-019-2593-x.
[54] T. Groń, Influence of vacancies and mixed valence on the transport processes in solid solutions with the spinel structure, Philos. Mag. B 70 (1994) 121–132, https://doi.org/10.1080/01418639408240200. Phys. Condens. Matter; Stat. Mech. Electron. Opt. Magn. Prop.
[55] H. Duda, I. Jendrzejewska, T. Groń, S. Mazur, P. Zajdel, A. Kita, Influence of vacancies on the electrical properties of the $ZnCr_{2-x}Ni_xSe_4$ spinels, J. Phys. Chem. Solids 68 (2007) 80–86, https://doi.org/10.1016/j.jpcs.2006.09.002.
[56] M.P. Ghosh, S. Mandal, S. Mukherjee, Correlations between microstructural and magnetic properties of $Gd^{3+}$-doped spinel ferrite nanoparticles, Eur. Phys. J. Plus 135 (2020), https://doi.org/10.1140/epjp/s13360-020-00112-5.
[57] J.L. Ortiz-Quiñonez, U. Pal, M.S. Villanueva, Structural, magnetic, and catalytic evaluation of spinel Co, Ni, and Co-Ni ferrite nanoparticles fabricated by low-temperature solution combustion process, ACS Omega 3 (2018) 14986–15001, https://doi.org/10.1021/acsomega.8b02229.
[58] M.A. Han, H.J. Kim, H.C. Lee, J.S. Park, H.N. Lee, Effects of porosity and particle size on the gas sensing properties of $SnO_2$ films, Appl. Surf. Sci. 481 (2019) 133–137, https://doi.org/10.1016/j.apsusc.2019.03.043.
[59] S. Ayyappan, S. Mahadevan, P. Chandramohan, M.P. Srinivasan, J. Philip, B. Raj, Influence of $Co^{2+}$ Ion concentration on the size, magnetic properties, and purity of $CoFe_2O_4$ Spinel ferrite nanoparticles, J. Phys. Chem. C 114 (2010) 6334–6341, https://doi.org/10.1021/jp911966p.
[60] V.K. Lakhani, T.K. Pathak, N.H. Vasoya, K.B. Modi, Structural parameters and X-ray Debye temperature determination study on copper-ferrite-aluminates, Solid State Sci. 13 (2011) 539–547, https://doi.org/10.1016/j.solidstatesciences.2010.12.023.
[61] I. Sharifi, H. Shokrollahi, M.M. Doroodmand, R. Safi, Magnetic and structural studies on $CoFe_2O_4$ nanoparticles synthesized by co-precipitation, normal micelles and reverse micelles methods, J. Magn. Magn. Mater. 324 (2012) 1854–1861, https://doi.org/10.1016/j.jmmm.2012.01.015.
[62] H. Zhang, D. Zeng, Z. Liu, The law of approach to saturation in ferromagnets originating from the magnetocrystalline anisotropy, J. Magn. Magn. Mater. 322 (2010) 2375–2380, https://doi.org/10.1016/j.jmmm.2010.02.040.

[63] S.W. Da Silva, F. Nakagomi, M.S. Silva, A. Franco, V.K. Garg, A.C. Oliveira, P. C. Morais, Effect of the Zn content in the structural and magnetic properties of $Zn_xMg_{1-x}Fe_2O_4$ mixed ferrites monitored by Raman and Mössbauer spectroscopies, J. Appl. Phys. 107 (2010), https://doi.org/10.1063/1.3350903.

[64] L. Yang, Z. Wang, B. Zhai, Y. Shao, Z. Zhang, Y. Sun, J. Yang, Magnetic properties of $Eu^{3+}$ lightly doped $ZnFe_2O_4$ nanoparticles, Ceram. Int. 39 (2013) 8261–8266, https://doi.org/10.1016/j.ceramint.2013.04.011.

[65] A. Hakeem, T. Alshahrani, G. Muhammad, M.H. Alhossainy, A. Laref, A.R. Khan, I. Ali, H.M. Tahir Farid, T. Ghrib, S.R. Ejaz, R.Y. Khosa, Magnetic, dielectric and structural properties of spinel ferrites synthesized by sol-gel method, J. Mater. Res. Technol. 11 (2021) 158–169, https://doi.org/10.1016/j.jmrt.2020.12.064.

[66] S. Güner, I.A. Auwal, A. Baykal, H. Sözeri, Synthesis, characterization and magneto optical properties of $BaBi_xLa_xY_xFe_{12-3x}O_{19}$ ($0.0 \leq x \leq 0.33$) hexaferrites, J. Magn. Magn. Mater. 416 (2016) 261–268, https://doi.org/10.1016/j.jmmm.2016.04.091.